

Actuation of Micro-Optomechanical Systems Via Cavity-Enhanced Optical Dipole Forces

Matt Eichenfield,^{1,*} Christopher P. Michael,¹ Raviv Perahia,¹ and Oskar Painter¹

¹Thomas J. Watson, Sr. Laboratory of Applied Physics, California Institute of Technology, Pasadena, CA

(Dated: April 24, 2019)

We demonstrate an optomechanical system employing a movable, micron-scale waveguide optically-coupled to a high- Q optical microresonator. We show that milliwatt-level optical powers create micron-scale displacements of the input waveguide. The displacement is caused by a cavity-enhanced optical dipole force (CEODF) on the waveguide, arising from the stored optical field of the resonator. The CEODF is used to demonstrate tunable cavity-waveguide coupling at sub-mW input powers, a form of all-optical tunable filter. The scaling properties of the CEODF are shown to be independent of the intrinsic Q of the optical resonator and to scale inversely with the cavity mode volume.

Although light is usually thought of as imponderable, carrying energy but relatively little momentum, light can exert a large force per photon if confined to small structures. Such forces have recently been proposed^{1,2} as a means to construct novel optomechanical components such as tunable filters, couplers, and lasers. Other theoretical studies of the nonlinear dynamics of these systems have shown them to be useful for performing optical wavelength conversion and efficient optical-to-mechanical energy conversion^{3,4}. In the field of quantum physics, there has also been recent interest in using radiation pressure forces within micro-optomechanical resonators to help cool macroscopic mechanical oscillators to their quantum-mechanical ground state^{5,6,7,8}. Here, we demonstrate an optomechanical system employing a movable, micron-scale waveguide optically-coupled to a high- Q optical microresonator. We show that milliwatt-level optical powers create micron-scale displacements of the input waveguide. The displacement is caused by a cavity-enhanced optical dipole force (CEODF) on the waveguide, arising from the stored optical field of the resonator. The CEODF is used to demonstrate tunable cavity-waveguide coupling at sub-mW input powers, a form of all-optical tunable filter. Finally, the scaling properties of the CEODF are shown to be independent of the intrinsic Q of the optical resonator, and to scale inversely with the cavity mode volume, indicating that such forces may become even more effective as devices approach the nanoscale.

The ponderomotive effects of light within optical resonators have long been considered in the field of high-precision measurement⁹. The canonical system, shown in Fig. 1a, consists of a Fabry-Perot (FP) resonant cavity formed between a rigid mirror and a movable mirror attached to a spring or hung as a pendulum¹⁰. A nearly-resonant optical field builds up in amplitude as it bounces back-and-forth between the mirrors and pushes on the movable mirror with each reflection, which detunes the FP cavity. The nonlinear dynamics associated with the displacement of the mirror and the build-up of internal cavity energy result in an “optical spring” effect¹¹. Under conditions in which the optical field cannot adiabatically follow the mirror movement, the radiation pressure force can drive or dampen oscillations of the position of the movable mirror^{12,13,14}—this effect is the basis for some optomechanical cooling schemes^{5,7,8}.

In contrast to the FP optomechanical system, the system studied here consists of a monolithic, whispering-gallery-mode (WGM) resonator coupled to an external waveguide. The waveguide is suspended (secured at two distant points) and behaves as if attached to a spring. Light evanescently couples into the resonator from the waveguide, as illustrated in Fig. 1b. The intra-cavity light intensity changes the waveguide position via an all-optical force on the waveguide due to the field of the resonator. The resulting movement changes the waveguide-resonator coupling-rate—rather than the cavity resonance condition as in the FP system—which is sensitive to the distance between the waveguide and resonator. Unlike the FP system, the optical force is derived from the gradient force, which is proportional to the gradient of the optical field.

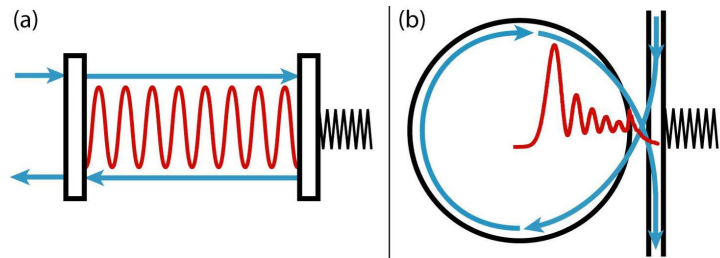


FIG. 1: Schematic diagrams of two different optomechanical cavity systems. Blue arrows indicate the propagation of light, with the resulting intensity profiles in the resonators shown as red lines. **a**, Fabry-Perot cavity system with the position of the back mirror behaving as a mechanical oscillator. Radiation pressure from the stored cavity field pushes on the reflective back mirror, causing a power-dependent nonlinearity in the length of the cavity. **b**, Evanscently-coupled cavity system. The position of the input waveguide acts as a mechanical oscillator in this case. A CEODF from the stored internal field of the resonator attracts the input waveguide, causing a power-dependent nonlinearity in the coupling of the waveguide to the cavity.

tween the FP system and the system in Fig. 1b can be made due to the external nature of the waveguide (the FP would require a mirror that could change its reflectivity in response to changing optical power¹⁷). This non-trivial difference also applies to a wide class of cavity geometries in which a non-resonant dielectric object loads the cavity.

In this work, the implementation of the optomechanical system of Fig. 1b consists of a high- Q silicon nitride (SiN_x) microdisk resonator of diameter $D = 44.8 \mu\text{m}$ and thickness $t = 253 \text{ nm}$. The resonator is fed optical power through an external waveguide formed from a micron-scale silica optical fiber taper. An optical micrograph of the micron-scale fiber taper in the near-field of the SiN_x microdisk is shown in Fig. 2b, indicating the geometry of the taper-disk coupling. Fabrication of the microdisk and the taper are described in detail elsewhere^{18,19}.

Figure 2a shows the transmission spectrum of a high- Q WGM of the microdisk at low (inset) and high power. At low powers ($< 1 \mu\text{W}$), the microdisk system behaves linearly. At higher powers, heating effects due to linear optical absorption within the SiN_x microdisk result in thermo-optic bistability. In addition to the thermo-optic effect (which gives rise to an asymmetric, shark-fin-like feature in the transmission spectrum²¹), the on-resonance transmission depth changes significantly with input power. This effect can be visually correlated with movement of the waveguide on a magnified microscope image such as Fig. 2c-d. Displacements on the order of the diameter of the waveguide ($1.1 \mu\text{m}$) can be produced with an incident power of 2.5 mW . The waveguide always moves towards the edge of the microdisk, with the movement disappearing when the waveguide is positioned far from the microdisk.

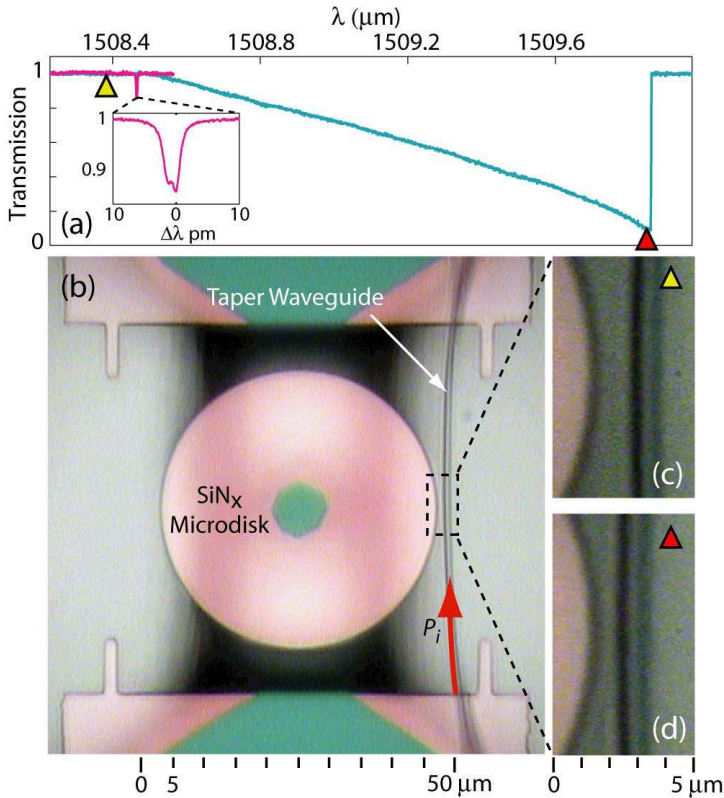


FIG. 2: Waveguide displacement. **a**, (inset) Low power ($< 1 \mu\text{W}$) linear transmission spectrum of a high- Q WGM of the microdisk (the slight “doublet” character of the mode spectrum is a result of surface-scattering-induced modal coupling of degenerate clockwise and counterclockwise WGMs²⁰). High power (2.5 mW) transmission spectrum (same mode as inset) showing thermo-optic bistability and a change in on-resonance transmission depth. The yellow(red) marker indicates the transmission level in panel c(d). **b**, Low-magnification, top-view image showing the microdisk-taper system. **c**, High-magnification image of the taper-disk coupling region taken at low optical input power, while the system is undercoupled. **d**, High-magnification image taken at high input power near resonance and critical coupling, showing a significant deflection of the taper waveguide towards the disk resonator.

the waveguide due to the polarization induced by the field of the resonator. Using complex fields and assuming linear dielectric susceptibility, the time-averaged polarization energy of the waveguide due to a dipole moment per unit volume $\mathbf{P}(\mathbf{r})$ is

$$\Phi = -\frac{1}{2} \int_{V_{\text{wg}}} \mathbf{P}(\mathbf{r}) \cdot \mathbf{E}_M^*(\mathbf{r}) d^3\mathbf{r} = -\frac{\epsilon_0 \chi_{\text{WG}}}{2} \int_{V_{\text{wg}}} |\mathbf{E}_M(\mathbf{r})|^2 d^3\mathbf{r}, \quad (1)$$

where V_{WG} is the geometric volume of the dielectric waveguide, χ_{WG} is the waveguide material’s electric susceptibility and $\mathbf{E}_M(\mathbf{r})$ is the electric field of the microdisk WGM. The average stored cavity energy, U , can be related to an effective mode volume of the WGM, $V'_M = 2U/n_M^2 \max[|\mathbf{E}_M(\mathbf{r})|^2]$, where n_M is the refractive index of the resonator. All the information of field amplitudes is carried in U and V'_M , which allows one to write

$$\Phi = -\frac{\chi_{\text{WG}} U}{n_M^2 V'_M} \int_{V_{\text{WG}}} |\hat{\mathbf{E}}_M(\mathbf{r})|^2 d^3\mathbf{r}, \quad (2)$$

where $\hat{\mathbf{E}}_M(\mathbf{r})$ is the unitless electric field eigenfunction of the WGM,

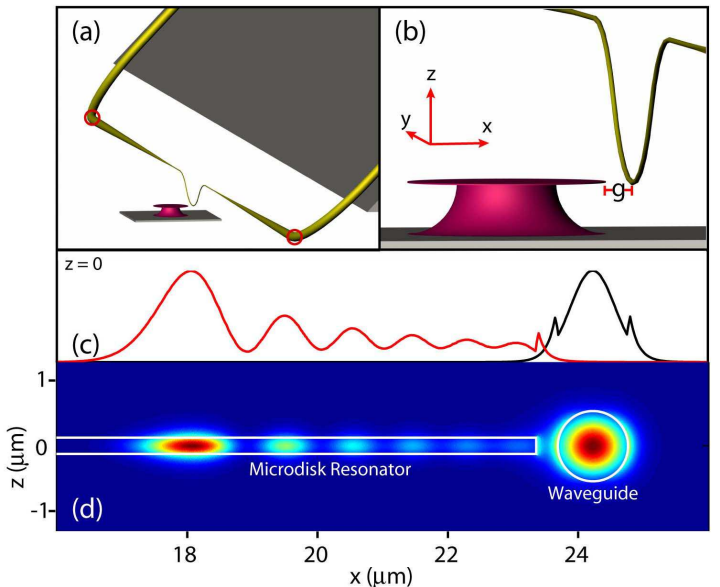


FIG. 3: Physical structure and fields of the waveguide-resonator system. **a**, Three-dimensional schematic view of the waveguide-resonator system. The tapered waveguide behaves roughly like a guitar string, pinned at the corners of the “U” (marked by red circles). **b**, Zoomed-in view of the waveguide-resonator system with coordinate reference. **c**, Projection of $|\hat{\mathbf{E}}_M(\mathbf{r})|^2$ along the x -axis for the WGM (red) and waveguide mode (black). **d**, Color-contour plot of $|\hat{\mathbf{E}}_M(\mathbf{r})|^2$ in the x - z plane; the physical boundaries are highlighted in white.

we find $V'_M = 159(\lambda_0/n_M)^3$ for the WGM of resonance wavelength $\lambda_0 = 1508.5 \text{ nm}$ studied here (see Methods).

In the limit of small parasitic losses²², the steady-state internal energy in the microdisk resonator is given by, $U = (1 - T)Q_M P_i/\omega$, where P_i is the input power in the waveguide at the resonator; ω is the angular frequency of the input light; Q_M is the intrinsic quality factor of the WGM; and T is the fractional waveguide transmission past the cavity. Fitting the spectrum of the WGM yields an unloaded, intrinsic Q -factor of $Q_M = 1.1 \times 10^6$.

The on-resonance transmission ($T_{\text{on}} = T(\omega_0)$) depends on the cavity-waveguide optical coupling- and loss-rates, $T_{\text{on}} = [(1 - \gamma_e/\gamma_i)/(1 + \gamma_e/\gamma_i)]^2$, where γ_e is the extrinsic (waveguide-to-resonator) coupling-rate, and $\gamma_i = \omega_0/Q_M$ is the intrinsic cavity loss-rate²³. The fields of both the microdisk resonator and the taper waveguide decay exponentially outside of their geometric boundaries due to the evanescent nature of the fields there (see Figs. 3(c-d)). We thus expect γ_e to vary exponentially with the disk-taper gap, g (shown in Fig. 3b); i.e. $\gamma_e(g) = \gamma_e(0) \exp(-\eta g)$, where $\gamma_e(0)$ is nominally the “zero-gap” coupling-rate. In Fig. 4b we plot $\gamma_e(g)$ as extracted from the measured $T_{\text{on}}(g)$ curve in Fig. 4a and unloaded Q -factor of the microdisk. $\gamma_e(g)$ shows the expected exponential dependence with gap, yielding a decay constant equal to $\eta = 1/206 \text{ nm}^{-1}$ for the disk-taper system. The fully-characterized low-power transmission curve (Fig. 4a), can be used to infer the relative disk-taper gap from any value of on-resonance transmission, T_{on} , given knowledge of whether the system is overcoupled or undercoupled.

Substituting in the exponential dependence of coupling on gap, one arrives at a dipole potential energy of the waveguide given by,

$$\Phi = -\frac{4\chi_{\text{WG}} \gamma_e(0) Q_M^2 P_i}{\omega_0^2 n_M^2 V'_M} \frac{e^{-\eta g}}{\left(1 + \frac{\gamma_e(0) Q_M}{\omega_0} e^{-\eta g}\right)^2} \int_{V_{\text{WG}}} |\hat{\mathbf{E}}_M(\mathbf{r})|^2 d^3\mathbf{r}. \quad (3)$$

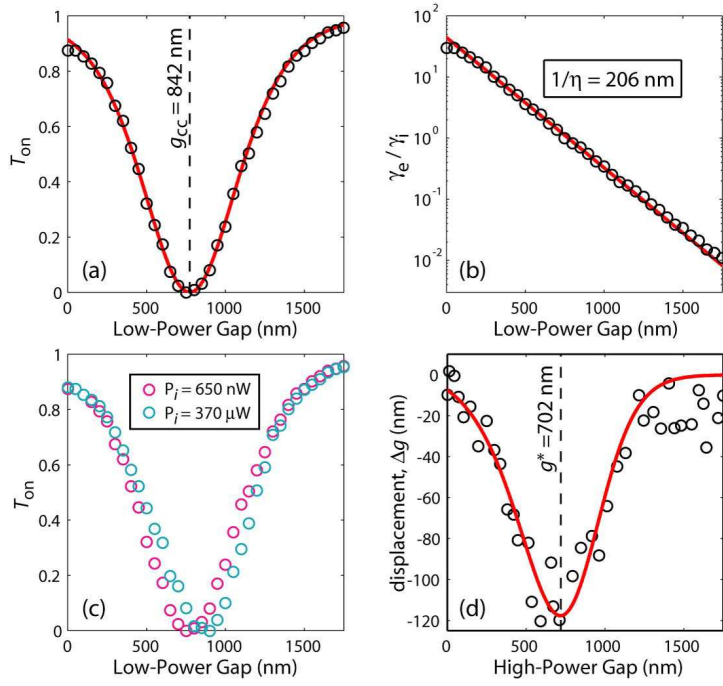


FIG. 4: Characterization of optical coupling and measurement of the CEODF. **a**, Measured transmission curve at low power, T_{on} vs. g , for the microdisk-taper system (a fit assuming exponential dependence of coupling on gap is shown as a solid blue line). **b**, γ_e/γ_i and fit extracted from (a) showing exponential dependence of coupling on gap. **c**, T_{on} vs. low-power gap for high (cyan) and low (magenta) input powers. **d**, Inferred Δg vs. high-power gap (equivalent to F_o/k_s). The actual high-power taper-disk gap is extracted from the fit to the low power coupling curve in panel a. The fit theoretical model of the CEODF is shown as a solid red line.

where σ is an effective decay constant, and V'_{WG} is an effective volume of the waveguide. In what follows, we take $\sigma \approx \eta$, as predicted by a simple coupled-mode theory of the taper-microdisk system²⁴ (as shown below, this assumption is borne out by experiment).

Although the amount of externally-coupled energy changes with the gap, the fast response rate of the optical cavity (0.88 ns photon lifetime) allows the resonator dynamics to be adiabatically removed. In this approximation, $\Phi(g)$ describes a completely conservative energy landscape without hysteretic or dissipative characteristics. The effective optical force on the waveguide is,

$$F_o(g) = -\frac{\partial\Phi(g)}{\partial g} = -\frac{8\eta V'_{WG}\chi_{WG}\gamma_e(0)Q_M^2 P_i}{\omega_0^2 n_M^2 V'_M} \frac{e^{\eta g}}{\left(e^{\eta g} + \frac{\gamma_e(0)Q_M}{\omega_0}\right)^3}. \quad (4)$$

We note that this force curve is significantly different from that of a closed system in which the optical dipole force would be given by the product of the stored cavity energy and the gradient of the microdisk mode's evanescent near-field intensity profile. The maximum of this force occurs at a gap $g^* = \eta^{-1} \ln[\gamma_e(0)Q_M/2\omega_0]$, and is given by

$$F_o^* = F_o(g^*) = -\frac{32\eta\chi_{WG}}{27n_M^2\gamma_e(0)} \frac{V'_{WG}}{V'_M} P_i, \quad (5)$$

In this model, g^* occurs on the overcoupled side of the critical coupling gap—not at $g_{cc} = \eta^{-1} \ln[\gamma_e(0)Q_M/\omega_0]$, the point of maximum stored cavity energy.

To test the validity of the model, we measure the position-dependence of the stored state from. Starting with the waveguide

move the resonator toward the waveguide in 50 nm steps using an encoded DC motor stage. At each position of the motor, we measure T_{on} at 650 nW and 370 μ W. Figure 4c shows the high- (cyan) and low-power (magenta) transmission curves. The actual position of the waveguide in the high-power measurement is extracted from the low-power T_{on} data. The change in actual waveguide-resonator gap, Δg , between the low- and high-power transmission curves is proportional to the force required to move the waveguide to its high-power position, assuming the mechanical spring constant (k_s) of the optomechanical system is linear. Thus, Fig. 4d is a plot of $F_o(g)/k_s$.

Figure 4d shows the fit to the force curve data using equation (4). As mentioned above, coupled mode theory predicts that $\sigma \approx \eta$; this equality is confirmed here as $\sigma/\eta = 1.01 \pm 0.03$ is the best nonlinear least-squares fit to the measured force curve when σ is left as a free parameter. The fit model also matches the measured recovery to zero force for small gaps, and has a peak force position ($g^* = 702$ nm), just on the overcoupled side of the zero transmission gap ($g_{cc} = 842$ nm). The numerical evaluation of the optical force in equation (4) yields a prediction for the magnitude of the optical force on the taper waveguide and, from the fit of the measured force curve in Fig. 4d, an estimate of the taper's mechanical spring constant. We find a peak optical force of 20 pN/mW of input power for the disk-taper system under study and a taper spring constant of $k_s = 73$ pN/ μ m.

Direct measurements of the mechanical properties of the taper waveguide were also performed. A diagram illustrating the geometry of the fiber taper waveguide used in these experiments is given in Figs. 3(a-b). Imaging of the fiber taper displacement with a microscope indicates that the optically-excited mechanical resonance of the taper is similar to the fundamental mode of an elastic wire, pinned at the corners of the “U”-shaped bend in the taper waveguide. As shown, the fiber taper waveguide is not a simple “U” shape, but rather has a small “dimple” (~ 160 μ m radius of curvature) at the taper's center to allow local probing of planar devices¹⁹. The torsional mode of the “dimple” does not appear to be excited. From the measured mechanical frequency ($\Omega = 2\pi \times 193$ Rad/s) and the physical mass of the taper's “U” section ($m = 2.6 \times 10^{-11}$ kg), we arrive at $k_s \approx 38$ pN/ μ m (see Methods). This value differs by less than a factor of three from the optically-measured spring constant of the taper waveguide.

Applications of the CEODF include optical control of micro- and nano-optomechanical devices for the dynamic switching, filtering, or modulation of light. Figure 5a shows the schematic of a simple experiment to demonstrate all-optical tuning of the filter characteristics of the microdisk using the CEODF. In this scheme a red control field ($\lambda_C \approx 1527$ nm) counterpropagates with a blue signal field ($\lambda_S \approx 1492$ nm), each of the fields resonant with a different mode of the microdisk (in this case, WGMs of the same radial order but azimuthal mode number difference $\delta m = 4$). The waveguide is pulled towards the resonator in proportion to the dropped control power, tuning the cavity-waveguide system from the undercoupled regime towards the overcoupled regime. In this way, the filter rejection level at the signal wavelength can be tuned by the control power level, as shown in Figs. 5(b-c). Using the thermo-optic bistability of the system, variation in the dropped control power is accomplished not by tuning the control power level, but rather by tuning the wavelength of the control laser. This provides an approximately linearly-tunable control; however, the resonance position for the signal is tuned simultaneously and must be tracked. By engineering a similar system in which the threshold power for thermo-optic bistability is much larger than the threshold power for optomechanical modulation, the same basic structures could be made to tune the cavity's filter properties by adjusting only the input power of the control—without the need to track the signal resonance. Utilizing a microfabricated on-chip resonator²⁵ to implement a system with high mechanical frequency

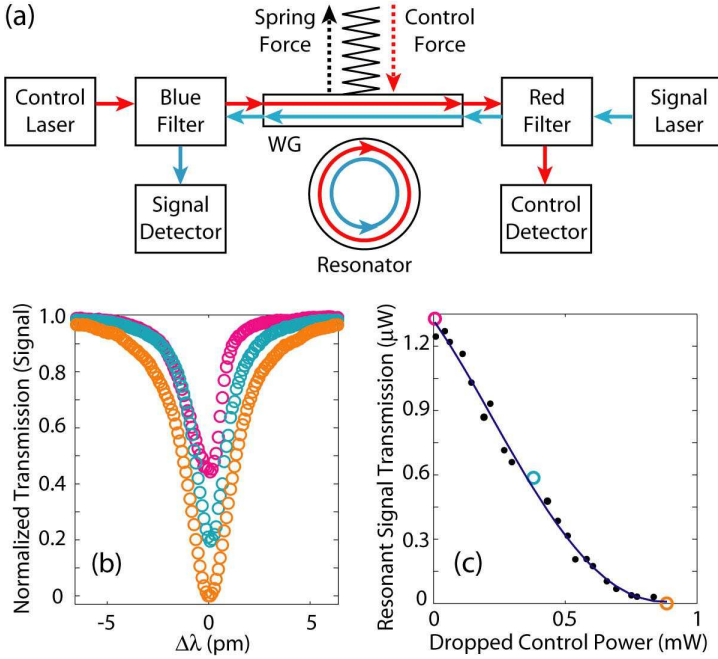


FIG. 5: Optically tunable filter demonstration. **a**, Experimental setup of the filter demonstration. **b**, Transmission spectrum of the signal field for three different dropped control powers. **c**, On-resonance transmitted signal power vs. dropped control power (with trend line). The signal extinction ratio is 21 dB for 0.9 mW of control power. Transmission spectra in panel b are taken at the dropped control powers indicated by open circles of matching color.

tuning or signal modulation.

Analysis of equation (5) indicates that the magnitude of the force does not scale with the intrinsic optical Q -factor (Q_M). This is a result of the interplay between the stored optical energy and the degree of cavity loading: increasing Q_M moves $g^* \sim \ln[Q_M]$ further from the disk, which exactly cancels the Q -enhancement of the internal field. The Q_M -independence of the force facilitates making systems insensitive to other nonlinearities which scale with Q_M (such as the thermo-optic bistability of the current devices). Indeed, early results with low- Q microdisks ($Q_M \sim 4100$) of roughly the same size ($D = 20 \mu\text{m}$) show large optical force effects with no observable thermo-optic bistability. Equation (5) also shows that the force scales inversely with V'_M . Therefore smaller devices, even with lower quality factors, give rise to a larger maximum force. Up to a factor of order unity, $V'_{\text{WG}}/\gamma_e(0)$ cancels, keeping the above scaling valid as devices approach the nano-scale. For example, in the case of planar two-dimensional photonic crystal nanocavities²⁸ with cubic-wavelength-scale mode volumes, the optical forces can be ex-

pected to be two orders of magnitude larger than in the microdisk studied here, approaching the nN level. Such scaling behavior is applicable to a wide variety of geometries in which the CEODF acts on non-resonant dielectric objects in the near-field of the optical resonator and indicates an interesting path towards low-power, high-speed micro- and nano-scale actuators and transducers.

Methods

The fiber taper is created by locally heating (with a H_2 torch) and drawing a standard SMF-28e silica fiber. An adiabatic taper is formed with a long (4 mm), narrow diameter region ($d = 1.1 \pm 0.1 \mu\text{m}$) in which the evanescent field of the guided mode penetrates significantly into the air cladding. The fiber is then bent in a "U"-shape²⁹, with the tapered region at the end of the "U" and the two fiber ends separated by an adjustable gap to provide varying tension levels to the taper. In addition, a "dimpled" region is created in the geometric center of the "U" region in order to access the disk, which resides in a trench. The fiber tension is mechanically adjustable; tension is optimized to accentuate optically-induced fluctuations while maintaining the waveguide's stability (the stability of the taper waveguide is exemplified in Fig. 4a).

Fiber-pigtailed, external cavity, tunable lasers operating over the 1400 and 1500 nm wavelength bands are used to couple optical power into the taper waveguide. The polarization of the guided mode in the taper is controlled via three adjustable fiber loops. Excitation of the whispering-gallery modes (WGMs) of the microdisk is performed by positioning the fiber taper in the equatorial plane of the microdisk and approaching the near-field of the microdisk from the side. Positioning of the disk (x - y) and taper (z) is accomplished using DC motors with $50 \pm 0.5 \text{ nm}$ encoded resolution.

The low-power T_{on} data in Fig. 4c allows the construction of a transmission curve that is identical to the transmission curve in Fig. 4a; it is nevertheless taken again, concurrently with the high power data, to cancel any drift in the taper-disk gap over the course of the measurement.

The particular WGM used in this study has six radial antinodes ($p = 6, m = 109, v = 0$; shown in Fig. 3c-d juxtaposed to the waveguide mode) and was chosen due to its high intrinsic (unloaded) Q and favorable taper-coupling characteristics (phase-matching). Individual WGM modes can be identified³⁰ via the following characteristics: the free-spectral range between modes, the radiation-limited Q of modes, and the strength of coupling to the taper waveguide (degree of phase-matching). The experimentally measured quantities are matched to accurate FEM simulations of the disk modes. The mode's identification was experimentally verified by moving the waveguide over the surface of the disk and measuring the characteristic radial pattern of the mode through changes in the taper-disk coupling-rate, γ_e .

We measured the mechanical resonance frequency by driving the taper waveguide with an electro-acoustical transducer in close proximity to the waveguide. The response of the waveguide appears as a clearly-visible oscillation in the on-resonance optical transmission of the cavity-waveguide system, well above the noise floor. By measuring this response against the frequency of the driving waveform, we extract the mechanical resonance frequencies. The effective mass of the oscillator is approximated by the mass of the fused-silica taper (length 8 mm, diameter exponentially tapering from 1.1 to 10 μm) weighted by the fundamental mechanical eigenfunction.

Acknowledgements

The authors sincerely thank Thomas Johnson, Paul Barclay, and Kartik Srinivasan for many fruitful discussions and helpful feedback.

* Electronic address: matt@caltech.edu

¹ M. L. Povinelli, M. Loncar, M. Ibanescu, E. J. Smythe, S. G. Johnson, F. Capasso, and J. D. Joannopoulos, *Opt. Lett.* **30**, 3042 (2005).

² M. L. Povinelli, S. G. Johnson, M. Loncar, M. Ibanescu, E. J. Smythe, F. Capasso, and J. D. Joannopoulos, *Opt. Express* **13**, 8287 (2005).

³ M. Notomi and S. Mitsugi, *Phys. Rev. A* **73**, 051803(R) (2006).

⁴ M. Notomi, H. Taniguchi, S. Mitsugi, and E. Kumanochi, *Phys. Rev. Lett.* **97**, 023903 (2006).

⁵ S. Gigan, H. R. Böhme, M. Paternostro, F. Blaser, G. Langer, J. B. Hertzberg, K. C. Schwab, D. Bäuerle, M. Aspelmeyer, and A. Zeilinger, *Nature* **444**, 67 (2006).

⁶ D. Kleckner and D. Bouwmeester, *Nature* **444**, 75 (2006).

⁷ O. Arcizet, P.-F. Cohadon, T. Briant, M. Pinard, and A. Heidmann, *Nature* **444**, 71 (2006).

⁸ A. Schliesser, P. Del'Haye, N. Nooshi, K. Vahala, and T. Kippenberg, *Phys. Rev. Lett.* **97**, 243905 (2006).

⁹ V. B. Braginskii and A. B. Manukin, *Measurements of Weak Forces in Physics Experiments* (The University of Chicago Press, Chicago, IL, 1977).

¹⁰ A. Dorsel, J. McCullen, P. Meystre, E. Vignes, and H. Walther, *Phys. Rev. Lett.* **51**, 1550 (1983).

¹¹ P. Meystre, E. M. Wright, J. D. McCullen, and E. Vignes, *J. Opt. Soc. Am. B* **2**, 1830 (1985).

¹² A. Pai, S. Dhurandhar, P. Hello, and J.-Y. Vinet, *Eur. Phys. J. D* **8**, 333 (1999).

¹³ T. J. Kippenberg, H. Rohrschi, T. Carmon, A. Scherer, and K. J. Vahala, *Phys. Rev. Lett.* **95**, 033901 (2005).

¹⁵ J. P. Gordon and A. Ashkin, *Phys. Rev. A* **21**, 1606 (1980).

¹⁶ H. J. Metcalf and P. van der Straten, *Laser Cooling and Trapping*, Graduate Texts in Contemporary Physics (Springer, New York, NY, 1999).

¹⁷ M. Fermann, F. Haberl, M. Hofer, and H. Hochreiter, *Opt. Lett.* **15**, 752 (1990).

¹⁸ P. E. Barclay, K. Srinivasan, O. Painter, B. Lev, and H. Mabuchi, *Appl. Phys. Lett.* **89**, 131108 (2006).

¹⁹ C. P. Michael, M. Borselli, T. J. Johnson, C. Chrystal, and O. Painter, *arxiv:physics/0702079* (2007).

²⁰ M. Borselli, T. J. Johnson, and O. Painter, *Opt. Express* **13**, 1515 (2005).

²¹ T. Carmon, L. Yang, and K. J. Vahala, *Opt. Express* **12**, 4742 (2004).

²² P. E. Barclay, K. Srinivasan, and O. Painter, *Opt. Express* **13**, 801 (2005).

²³ S. M. Spillane, J. C. Kippenberg, O. J. Painter, and K. J. Vahala, *Phys. Rev. Lett.* **91**, 043902 (2003).

²⁴ C. Manolatou, M. J. Khan, S. Fan, P. R. Villeneuve, H. A. Haus, and J. D. Joannopoulos, *IEEE J. Quan. Elec.* **35**, 1322 (1999).

²⁵ M.-C. Lee and M. C. Wu, *IEEE Phot. Tech. Lett.* **17**, 1034 (2005).

²⁶ X. M. H. Huang, C. A. Zorman, M. Mehregany, and M. L. Roukes, *Nature (London)* **421**, 496 (2003).

²⁷ T. Carmon and K. J. Vahala, *Phys. Rev. Lett.* (2007), in press.

²⁸ O. Painter, J. Vučković, and A. Scherer, *J. Opt. Soc. Am. B* **16**, 275 (1999).

²⁹ P. E. Barclay, K. Srinivasan, M. Borselli, and O. Painter, *Opt. Lett.* **29**, 697 (2004).

³⁰ M. Borselli, K. Srinivasan, P. E. Barclay, and O. Painter, *Appl. Phys. Lett.* **85**, 3693 (2004).